Slab-plate coupling via downbending and GPE

Dan Sandiford[1]*

[1] University of Sydney, AUSTRALIA
*Corresponding author (e-mail: dansandifordscience@gmail.com)

Abstract

The coupling between subducted slabs and trailing plates is often conceptualised in terms of a net in-plane force. If a significant fraction of upper-mantle slab buoyancy (e.g. 25%) were transferred in this manner, a net in-plane force on the order of 5-10 $\mathrm{TN\,m^{-1}}$ would be typical of the trailing plates. Results from a numerical subduction model are presented here which question both the magnitude and – perhaps more profoundly – the mode of force transmission. In this model the subducting plate (SP) driving force is predominantly supplied by differences in gravitational potential energy (GPE). The GPE associated with plate downbending (flexural topography) provides about half the total driving force. The magnitude of the trench GPE is related to the amplitude of topography, but is mediated by the internal stress distributions associated with bending. Above the elastic core, the stress is Andersonian and vertical normal stresses are lithostatic. This implies horizontal gradients in the vertical normal stress, across columns of different elevation in the outer slope. The bulk of the trench GPE arises from this upper, extensional section the lithosphere. Vertical shear stress (and horizontal gradients thereof) are concentrated in the elastic core of the slab, where principal stresses rotate through 90°. In this region, horizontal gradients in vertical normal stress rapidly diminish; they fully equilibrate at about twice the neutral plane depth. For the deepest trenches on Earth, these relationships imply trench GPE of up to about 5 $\mathrm{TN\,m^{-1}}$ The model demonstrates that mantle slabs can drive plate tectonics simply through downbending, where the predominant mode of slab-plate coupling is via the vertical shear force and bending moment.

1 Introduction

Slab pull is widely – although not universally – considered to be the dominant driving force for plate tectonics (e.g. Conrad and Lithgow-Bertelloni, 2002; Ghosh and Holt, 2012). The idea of direct coupling between the slab and the trailing plate is often attributed to Elasasser (1969), and was rapidly integrated into quantitative models (McKenzie, 1969). These early papers present the enduring idea of the downdip component of the slab buoyancy. It has become commonplace to depict this downdip force as a vector that simply follows the slab, through the hinge, ultimately applying a horizontal pull on the trailing plate (Forsyth and Uyeda, 1975)

The buoyancy force associated with upper mantle slab density is very significant, typically a few times 10 $\mathrm{TN\,m^{-1}}$ (Turcotte and Schubert, 2002; McKenzie, 1969; Faccenna et al., 2012; Rowley and Forte, 2022). In this study I refer to "slab pull" as the residual of the (large) upper mantle slab buoyancy and the (uncertain) integrated tractions.While the buoyancy force must be vertical, the net effect of tractions need not be. Hence the residual (slab pull) may have a net horizontal component. The term "net slab pull" is used to describe the horizontal component of force acting on the trailing plate (i.e. as an edge force). The slab pull "reduction factor" is a term used to describe the conversion from the magnitude of upper mantle slab buoyancy, to net slab pull. A ballpark figure that seems to have emerged for this factor is about 25% (Faccenna et al., 2012; Stotz et al., 2018; Clennett et al., 2023; Rowley and Forte, 2022); this would imply net slab pull of the order of 5-10 TN m^{-1} for old lithosphere.

Slab-plate coupling is not restricted to stresses within the slab, as these downwellings are expected to drive mantle flow which also interacts with the surface plates (McKenzie, 1969; Conrad and Lithgow-Bertelloni, 2002; Husson, 2012). However, the focus of this paper is the coupling that occurs within the slab due to the assumed capacity to support significant deviatoric stresses ($O(100)$ MPa), relative to the upper mantle. A number of depth integrated quantities are commonly used in describing the loading: the net-in plane force (F_{net}), the shear stress resultant (V) and the bending moment (M). These are defined in Table 1. As defined in this study, the net slab pull is equal to F_{net} evaluated at the trench. There are several means by which slab plate coupling has been investigated and constrained; these constraints apply somewhat differently in terms of the vertical and horizontal coupling. Non-uniqueness is recognised in both cases (Solomon and Sleep, 1974; Davies, 1978; Becker and O'Connell, 2001).

The vertical component of the slab-plate coupling produces plate deflection and associated gravity anomalies (Watts and Talwani, 1974), and both of these can be relatively easily measured. However there is substantial non-uniqueness in inverting these observations for the vertical loading (e.g. V). This is because the amplitude of flexure can depend very strongly on the assumed mechanical properties of the plate, while also being a function of the bending moment (M). (Parsons and Molnar, 1976; Caldwell et al., 1976; Hunter and Watts, 2016; Garcia et al., 2019). The deflection for uniform elastic plates is proportional to T_e^{-3}, so for larger elastic thicknesses, much larger vertical shear stresses will be inferred. For instance, Zhang et al. (2023) infer V in the range 15-30 TN m^{-1} for the southern Marianas, which is close to the entire weight of the slab. However, it is doubtful that the lithosphere could support a loading pattern that requires an integrated vertical shear stress of this magnitude. Non-linear flexure models with an elastic-perfectly plastic rheology require V in the range of only 0.5-1.5 TN m^{-1} across Pacific Plate subduction zones (Turcotte et al., 1978).

The horizontal component of slab-plate coupling is related to longstanding questions about the torque balance of the surface plates. Key observations that can help constrain the torque balance relate to plate kinematics (velocities), intra-plate stress patterns, as well as changes in these quantities over time (Forsyth and Uyeda, 1975; Becker and O'Connell, 2001; England and Molnar, 2022). Several studies, both global and regional in extent, concluded that slab buoyancy is largely balanced by deep resistance, with slab pull reduction factors of $\sim$ 10 % (Forsyth and Uyeda, 1975; Wortel et al., 1991; Copley et al., 2010; England and Molnar, 2022; Wouters et al., 2021). In contrast, global-scale velocity modelling has favored high net slab pull (reduction factors $\geq$ 50 %) (Conrad and Lithgow-Bertelloni, 2002; van Summeren et al., 2012). However, consistent present-day velocity fields can be generated by global convection models, driven by the whole mantle density structure, but which do not include strong slabs (Steinberger et al., 2001; Ghosh and Holt, 2012). Investigation of intra-plate stress patterns has generally concluded that: 1) the whole mantle density structure can predict long wavelength features of the intra-plate stress field, without requiring strong slabs (Steinberger et al., 2001; Ghosh and Holt, 2012; Osei Tutu et al., 2018); 2) the typical magnitude of net slab pull is of the order of other shallow lithospheric density anomalies (e.g. ridge push) (Richardson et al., 1976; Richardson, 1992; Coblentz et al., 1994; Sandiford et al., 2005).

While the *magnitude* of both the vertical and horizontal component of slab-plate coupling are debated, the basic *mode* of coupling between slabs and trailing plates has been less controversial. The vertical coupling is though to be mediated through vertical shear stresses (with the bending moment also influencing the flexure). Meanwhile, the horizontal coupling is generally conceptualised in terms of a net in-plane force transmitted through the subduction hinge (the net slab pull). Of course, net slab pull cannot arise from buoyancy alone (Bird et al., 2008), and the concept relies on the assumption that integrated external tractions acting on the slab must have a net horizontal component. This may occur, for instance, if the slab-normal component of the buoyancy force was balanced by the pressure distribution outside the slab (McKenzie, 1969; Holt, 2022).

Subduction zone modelling (analytical, numerical and analogue) has provided some important insights into these issues. Several studies have concluded that slab buoyancy in such models is largely balanced by mantle drag, with inferred values of net slab pull being less than about 5 $\mathrm{TN\,m^{-1}}$, at least once the slab is supported by the lower mantle (Schellart, 2004; Capitanio et al., 2007, 2010; Sandiford et al., 2020). Such values have typically been estimated by integrating stresses seaward of the zone of bending. Other studies have reported that integrated basal drag is about 10% of the slab buoyancy force (Suchoy et al., 2021). This implies a slab pull reduction factor of a similar value. Models also show that a dominant component of the upper mantle drag is the pressure differential across the slab (Whittaker, 1988; Holt and Becker, 2016; Royden and Husson, 2006; Holt, 2022). In general, results of previous subduction zone models can be invoked to suggest that: a) net slab pull is predicted to be relatively low compared to total slab buoyancy; b) upper mantle flow-driven pressure differential could explain why the slab pull force has a net horizontal component (whereas the slab buoyancy force does not).

This study revisits the issue of slab-plate coupling and provides some additional insights. Most importantly, it shows that the coupling between slabs and plates need not occur via a horizontal net in-plane force; plates can be driven by mantle slabs simply through downbending, due to the generation of a gravitational potential energy difference. This style of slab-plate coupling, which predominantly occurs through vertical shear and bending moment, is remarkably similar to loading patterns inferred in static models of flexure (Turcotte et al., 1978; Hunter and Watts, 2016)). In section 2 I provide a brief overview of the numerical model, and discuss the thin-plate description of the horizontal force balance on the SP. In section 3.1 I use this approach to analyse the balance of driving and resisting forces on the SP. In section 3.2 I discuss the stress patterns in the bending plate and show how these control the magnitude of the trench GPE. The connections with previous studies, and some implications for global tectonics are discussed in Section 4.

2 Numerical model and method of analysis

The 2D numerical model was developed using the ASPECT code (version 2.2.0, see Heister et al. (2017); Kronbichler et al. (2012); Bangerth et al. (2020, 2023)). The model represents an idealised, quasi-steady state subduction configuration, where flow is driven solely by the thermal density structure of oceanic lithosphere (within both the slab and plates). At the initiation of the model, the age of the lithosphere at the trench is 100 Myr, and the temperature was prescribed by a half-space cooling profile. The numerical model is identical to that described in Sandiford and Craig (2023), which includes a detailed description of the model setup and parameters. Here, a brief high-level overview of the model is provided, focusing on the assumptions and limitations.

The model has free-slip conditions on the sides and base, and has a free surface. The water column is not included so that the isostatic restoring force is proportional to the density of the asphenspheric mantle ($\Delta\rho$, see Table 1). A total elevation difference of about 4.5 km is developed in the model, between ridge and trench. The model treats the mantle and lithosphere as an incompressible visco-elastic-plastic continua in static equilibrium. The constitutive model incorporates the classical model of oceanic lithosphere strength (e.g. Goetze and Evans, 1979). Elastic shear stresses are limited by the frictional strength of faults (Byerlee, 1978), as well as both power-law and exponential creep (Hirth and Kohlstedt, 2003; Mei et al., 2010). The deeper mantle deforms via a linear (diffusion creep) mechanism, which was implemented to follow radialviscosity constraints (Steinberger and Calderwood, 2006). The subduction interface is modeled in an *ad hoc* way (e.g. Sandiford and Moresi, 2019), by imposing a separate material in which the frictional strength is much lower ($\mu = 0.005$) than is assumed in the rest of the model ($\mu = 0.8$). The combination of these mechanisms leads to hierarchy of characteristic shear stresses: 1 MPa in the asthenosphere; 10s MPa in the subduction interface, as well as the lower mantle, and 100s MPa in cold part of the bending plate ($<$ 700°C).

Fig. 1 shows the model domain (4 x vertically exaggerated) at 5 Myr after the initiation time (the same step as discussed in Sandiford and Craig (2023)). The scalar field shows the effective strain rate. The white lines show streamlines of the velocity field. Fig. 2 shows several components of the stress field in the SP near the trench.

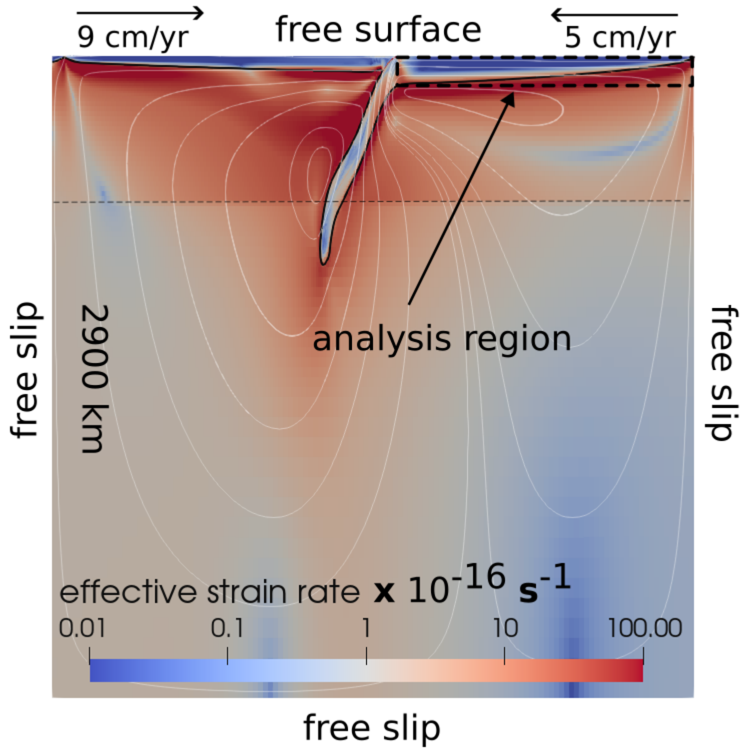

Figure 1: Subduction model domain, at 4$\times$ vertical exaggeration. Scalar field shows the effective strain rate. White lines are stream lines of the velocity. Solid black line shows the 1550 °C (potential temperature) contour. Dashed black line shows the region where the horizontal force balance is quantified. Effective strain rate refers to $\sqrt{\frac{1}{2}\dot{\epsilon}_{ij}\dot{\epsilon}_{ij}}$, where $\dot{\epsilon}_{ij}$ is the strain rate tensor.

The Stokes Equations, which are solved in the numerical model (by FEM), represent a solution to the stress equilibrium equations (subject to incompressibility) in the x and z directions:

$$\frac{\partial \tau_{xx}}{\partial x} - \frac{\partial P}{\partial x} + \frac{\partial \tau_{xz}}{\partial z} = 0 \tag{1}$$

$$\frac{\partial \tau_{zz}}{\partial z} - \frac{\partial P}{\partial x} + \frac{\partial \tau_{xz}}{\partial x} = -\rho g \tag{2}$$

The coordinate system is positive to the right (x) and positive up (z) (e.g. Fig 1), and compressive stresses are negative. To analyse the horizontal force balance on the SP, a thin-plate approach is used. The thin-plate analysis takes the model stress fields that satisfy the equilibrium equations, where dimensions are force per unit volume, and then integrates these over a sub-region that encompasses the plate (as shown in the white box in Fig. 1). Following integration, we have terms that a describe a balance of horizontal forces, with the dimensions of force per unit distance (N m^{-1}) in the out of plane direction. The derivation of this force-balance is included in Appendix 1. One of the steps in this analysis involves the substitution of the pressure in equation 2, in terms of vertical stress components, i.e., using $P = \tau_{zz} - \sigma_{zz}$. This step highlights the way in the which distribution of vertical stress is coupled to the horizontal force balance, through the effect on the pressure (and underlies the concept of gravitational potential energy gradients). The thin plate description of the horizontal force balance at point x is given by:

$$\int_{x_t}^{x} \tau_{xz}\Big|_L dx = -(\bar{\sigma}_{zz})\Big|_{x_t}^{x} - (\bar{\tau}_{xx} - \bar{\tau}_{zz})\Big|_{x_t}^{x} \tag{3}$$

Overbars represent the vertical integration from the surface ($s(x)$) to a reference level L, chosen here as 125 km relative to the ridge height. x_t is the trench location. A positive change in terms in equation 3 represent a force acting to the right on the lithosphere between x_t and x. The first term on the left represents the integrated effect of the basal shear stress from x_t to x. The first term on the right is the gravitation potential energy change. The second term is the (depth integrated) change in the “membrane stress”, representing the contribution of deviatoric stresses to the force balance (Bueler and Brown, 2009). For incompressible plane strain, $(\tau_{xx} - \tau_{zz}) = 2\tau_{xx}$. The depth integrated membrane stress is referred to as the net in-plane stress (F_{net}). In more symbolic notation, we can write:

$$\int_{x_t}^{x} \tau_{xz} dx = \Delta(GPE) - \Delta(F_{net}) \tag{4}$$

In this expression, the “GPE” has been defined as the negative of the depth integrated vertical stress. This means that a positive change in GPE represents a force to the left. This definition allows us to represent equation 4 as the variation in 3 positive quantities (as will be shown in Fig. 3). The integrals are estimated using interpolation and quadrature.

Turning to the vertical stress balance, integration of equation 2 from the surface ($s(x)$) to an arbitrary depth (z) yields the following:

$$\sigma_{zz}(x, z) = -\int_z^s \rho(x, z')g dz' - \frac{\partial}{\partial x}\int_z^s \tau_{xz} dz' \tag{5}$$

The terms on the right hand side are referred to as the lithostatic pressure $P(x, z)$ and the shear function $Q(x, z)$, ((e.g. Schmalholz et al., 2014), see Table 1). Assuming that: a) vertical stresses are balanced at the base of the lithosphere (L); and b) trench deflection is purely flexural in nature, we can write:

$$\frac{\partial}{\partial x}\bar{\tau}_{xz} = \bar{\rho}(z)g \approx \Delta\rho g w \tag{6}$$

This equation says that at the compensation depth, the force due to the horizontal gradient in integrated vertical shear stress is balanced by the isostatic restoring force, due to the flexural deflection of the lithosphere ($\Delta\rho g w$). This is simply the statement of the vertical force balance from thin plate flexure (Turcotte and Schubert, 2002). The integral of the vertical shear stress in that context called the shear stress resultant: $V = \bar{\tau}_{xz}$. Hence we can rewrite 6 as:

$$\frac{1}{\Delta\rho g}\frac{\partial}{\partial x}V \approx w \tag{7}$$

Equation 7 says that flexural topography (w) must be balanced by gradients in the vertical shear stress resultant (V) across the plate. However, it doesn't specify at what depths gradients in the vertical shear stress (i.e. Q) are concentrated. Because the vertical normal stress (σ_{zz}) depends on the shear function, and integrated vertical normal stresses appear in the horizontal force balance, the GPE associated with flexural topography will depend on the depth at which the shear function is concentrated.

Fig. 2 shows the variation of the membrane stress (top panel) and the vertical shear stress (bottom panel) proximal to the trench. The inset panel shows the orientation of the most compressive principal stress (σ_3). An important feature of the stress pattern is the systematic rotation of σ_3, which occurs across the "elastic core" (the region near the neutral plane, where differential stresses due to bending have not yet reached the yield limit). It can be seen that the depth extent of plastic yielding in the upper (extensional) part of the SP, strongly effects the distribution of vertical shear stress.

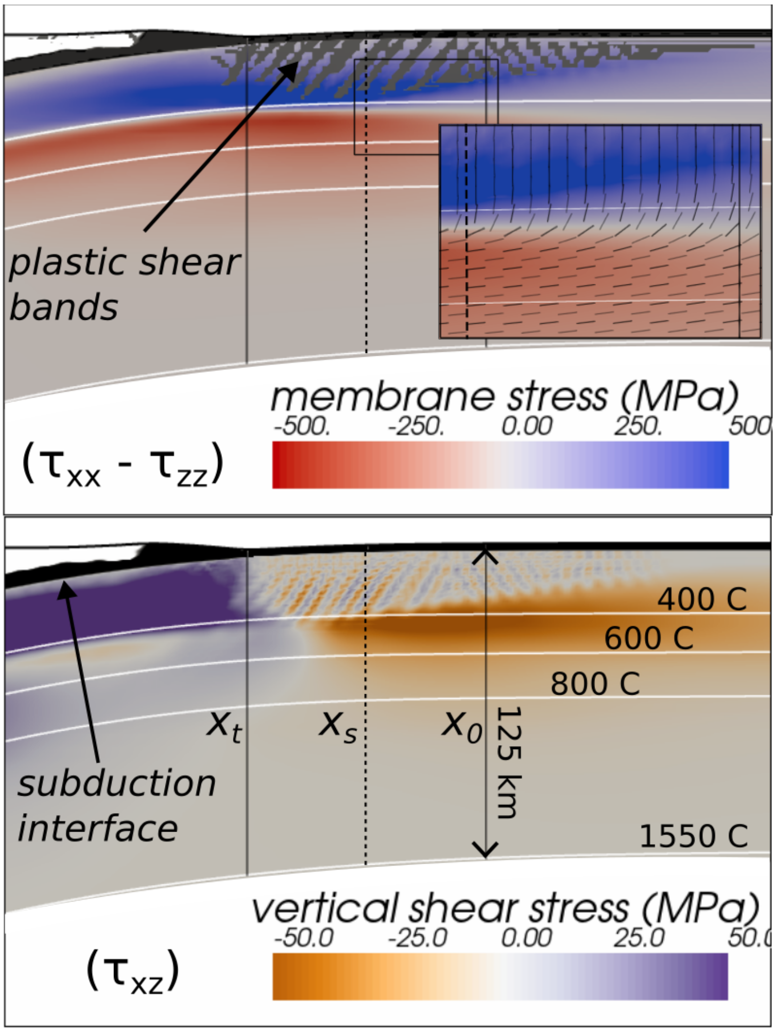

Figure 2: Distribution of the membrane stress (top panel) and vertical shear stress (bottom panel). Note that the scale of the 2 colorbars differs by an order of magnitude. The inset in the top panel shows a portion of the plate around the elastic core. Black bars in the inset panel show the orientation of the most compressive principal stress (magnitude not shown). Note the rotation of the principal stresses from vertical-above to sub-horizontal-below the core.

Name and symbol	Explanation	Related equation / value
SP/OP	subducting/overidding plate	-
$s(x)$	surface of plate	-
z_n	neutral plane depth	-
LAB	lithosphere-asthenoshere boundary	$\sim$ 125 km near trench
L	integration depth rel. to ridge height	125 km
-	membrane stress	$(\tau_{xx} - \tau_{zz})$
F_{net}	net (deviatoric) in-plane force	$F_{\mathrm{net}} = \int_L^{s(x)} (\tau_{xx} - \tau_{zz}) dz$
σ_1/σ_3	most extensive/compressive principal stress	
$\Delta\sigma$	differential stress	$\sigma_1 - \sigma_2$
M	bending moment	$\int_L^{s(x)} (z - z_n)(\tau_{xx} - \tau_{zz}) dz$
V	integrated vertical shear	$V = \int_L^{s(x)} \tau_{xz} dz.$
$\Delta\rho$	density of lithosphere at the LAB	3175 kg m^{-3}
$P(x,z)$	lithostatic pressure	$\int_z^s \rho(x,z')g dz'.$
$Q(x,z)$	shear function	$\frac{\partial}{\partial x} \int_z^s \tau_{xz} dz$
GPE	(-1 $\times$) integrated vertical normal stress	$-1 \int_L^{s(x)} \sigma_{zz} dz$

Table 1: Symbols and definitions used in this paper. For parameters used in the setup of the numerical model, see Sandiford and Craig (2023)

3 Results

3.1 The horizontal force balance

The variation of horizontal forces acting on the SP is shown in the main panel of Fig. 3. Solid lines show the variation of the 3 terms in the horizontal force balance (Eq. 4). The total basal resisting force (red line) is $\sim$ 4 TN m^{-1}. At the trench, the value of F_{net} is $\sim$ 0.5 TN m^{-1}, showing that net slab pull is small compared to the basal resisting force. Across the SP, 3 domains can be identified in which one of the terms in Eq. 3 can be disregarded (labelled d1, d2, d3). In d1, between the trench and the outer-rise, there is a rapid increase in GPE, on the order of 2 TN m^{-1}. The basal force across this $\sim$ 100 km section is minimal, so that the GPE change must nearly balance the increase in F_{net}. This increase means that the stress state becomes more extensional. In d2, the GPE is stationary, so that the gradient in F_{net} is negative (representing a force to right) with equal magnitude to the basal force contribution. In d3, near the ridge, F_{net} is close to zero and nearly stationary; here the GPE is balanced by the basal force contribution. Overall the driving force on the SP is dominated by GPE differences, while F_{net} functions to mediate the stress.

Another important aspect of the dynamics shown in Fig. 3 is the role of dynamic topography (DT). As discussed in Sandiford and Craig (2023), the SP topography deviates from the isostatic level by an amount (in total about $\sim$ 450 m) that very closely matches the gradient in pressure in the asthosphere (with a total variation of about 15 MPa across the 5000 km plate). Because this is a flow-driven pressure pattern, the topographic contribution is referred to as "dynamic" (see Schubert et al. (1978); Holt (2022) for further discussion). The flattening of the plate is shown in the top panel of Fig. 3. This tilt tends to oppose the GPE that would otherwise be generated from isostatic subsidence. The impact of the DT can estimated treating the force as a "slab on a slope" (e.g. Steinberger et al., 2001). Assuming an air-rock density difference of $\Delta\rho$, and a plate of thickness L, the horizontal component of the gravitational force due to DT is equal to:

$$dF_{DT} = \Delta\rho g L \frac{dh}{dx} dx = L\ dP \tag{8}$$

The sign choice is the same as used for GPE, with an increase in F_{dt} to the right, representing a net force to the left. The dashed blue line shown in Fig. 3 shows the total GPE minus the estimated contributions derived from Eq. 8. The total change in this "corrected GPE" is close to 3 TN m^{-1}, not including the trench-GPE component (where the line is shown with greater transparency). This is similar to the theoretical ridge push contribution (Turcotte and Schubert, 2002). Because the pressure gradient under the SP is related to driving the return flow to the ridge, and that return flow also contributes to the basal shear, the force due to the DT and the basal shear can be viewed as the dual interaction of the mantle flow with the plate (e.g. Steinberger et al., 2001).

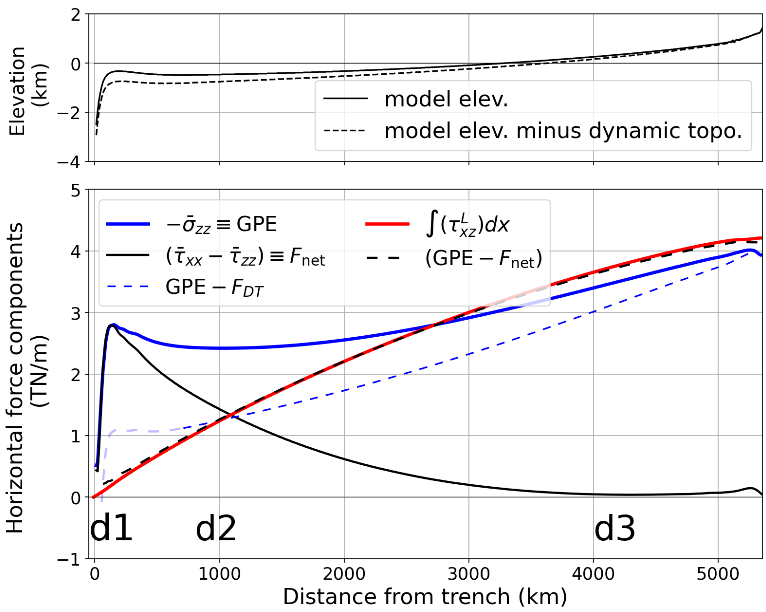

Figure 3: Top panel shows the model topography, as well as the topography corrected for the horizontal variation in "dynamic pressure" at the LAB depth (125 km). See Sandiford and Craig (2023) for further discussion. Solid lines in bottom panel show the variation of the 3 terms in the horizontal force balance (Eq. 4). An increase in GPE (towards the right) indicates a net force to the left. For all other terms, an increase is force to the right. The domains (d1, d2, d3) are discussed in the main text. The dashed black line shows the GPE minus the net in-plane force, positive values indicate total force acting to the left (the driving force), and must be balanced by the basal shear. The dashed blue line shows the GPE, with the estimated force contribution of dynamic topography (F_{DT}) removed. The GPE due to isostatic subsidence is reduced by almost a half, due to the effect of dynamic topography.

3.2 Controls on trench GPE

This section focuses on stress patterns in the bending plate, and the relationship between these patterns and the magnitude of the trench GPE. Fig.4 shows the key information required to address this problem. The most important feature of the stress pattern – and one of the key takeaways from this study – is that vertical shear stresses are concentrated within the elastic core.

Fig.4a-b highlights several key relationships between depth-integrated stress quantities. Fig.4a shows the horizontal variation in the bending moment (M) as well as the vertical shear stress resultant (V) in a ~ 300 km region seaward of trench. These two quantities are related by $\frac{dM}{dx} \sim V$, being the leading-order terms in the moment balance (e.g. Buffett and Becker, 2012). The bending moment saturates at about 25 km seaward of the trench, which is approximately the same location at which V changes sign. At the trench, the integrated vertical coupling (V) is ~ 1 TN m^{-1}. The (depth-integrated) vertical force balance equation (Eq. 7), states that horizontal gradients in V are equal to the isostatic restoring force due to the flexural topography. These two quantities are shown in Fig.4b, and are essentially identical apart from noise. This implies that the trench-outer-slope topography in the numerical model is a completely flexural feature (i.e. non-isostatic). The position labelled x_0 is referred to as the first zero crossing: this is a stationary point in dV/dx.

While Fig.4a&b show vertically-integrated quantities (e.g. M, V), Fig.4c-e shows the depth variation in the underlying components of the stress. Because there is noise in the stress components – a result of plastic shear banding in the yielding plate – stress quantities are averaged across a finite region (20 km), shown with a vertically-oriented grey band in Fig.4 a-b. The thick lines in Fig.4c-e show horizontally averaged stresses profiles, while the faint lines show individual profiles interpolated from the model.

Fig.4c shows the distribution of vertical shear stress with depth, which is negligible down to a depth of about 25 km, while a peak then occurs in the range of about 30-40 km. The red line in Fig.4d shows the depth distribution of the membrane stress, exhibiting the polarised pattern indicative of a bending-dominated stress state. Comparing Fig.4c&d, it is is clear that the peak in vertical shear stress coincides with the elastic core depth region (shown by the horizontally-oriented grey band). These features are explicable in terms of the orientation of the stress field. Above the elastic core stresses are Andersonian, so that while membrane stresses increase rapidly (Fig.4d) vertical shear stress remains close to zero. In the elastic core, the stress rotates through 90°, which implies finite shear stress on vertical planes, assuming the stress field retains a deviatoric component. Indeed, this rotation of the stress field can be seen in the inset panel of Fig. 2.

Further insight can be gained by comparing the membrane stress and the differential stress (Fig.4d). These quantities are equal, only when the stress state is Andersonian. The dashed green line in Fig.4d shows the magnitude of the differential stress ($\Delta\sigma$). Note that while $\Delta\sigma$ reduces in the elastic core, it does not go to zero (i.e. the stress field does retain a finite deviatoric component within the elastic core). $\Delta\sigma$ has a minimum of about 100 MPa, about twice the peak magnitude vertical shear stress (Fig.4c). This is consistent with the rotation of the stress such that within the core, vertical shear stress reaches a maximum (equal to half $\frac{1}{2}\Delta\sigma$) at the point where the principal stresses are oriented at 45 ° to the vertical. In terms of the vertical shear stress, the stress rotation dominates over the absolute reduction in the differential stress. The Supplementary Information shows that such stress rotations are characteristic of the interior region of bending plates, as evidenced in analytic solutions to the equilibrium equations.

Note that there is also non-negligible vertical shear stress in the yielding part of the plate beneath the elastic core (where stresses are limited by ductile creep). This indicates that the stress state beneath the neutral plane is not strictly Andersonian – a small deviation of the principal stresses away from vertical, combined with relatively large differential stress, results in non-negligible vertical shear stress. This can also be identified in the orientation of principal stress in the inset panel of Fig. 2.

Having discussed the distribution of vertical shear stress and its relation to the bending and yielding of the plate, the implications for the magnitude of the trench GPE can now be assessed. Recall that differences in GPE require horizontal differences in the vertical normal stress (Eq. 6). The vertical normal stress is controlled by both the lithostatic pressure (P) and the shear function (Q); if the shear function is zero the gradient in vertical normal stress will be lithostatic. Fig.4e shows the difference between the vertical normal stress averaged around x_s, and the vertical normal stress at a reference location x_0, where flexural topography is zero. In the region above the elastic core, the difference in vertical normal stresses is approximately constant, and equal to the pressure associated with the elevation difference: $\Delta\sigma_{yy} \sim w\Delta\rho g$, as labelled with the arrow in Fig.4e. This implies that above the elastic core vertical normal stresses in each column are approximately lithostatic, and thus the shear function plays a negligible role in the vertical force balance. In the depth range of the elastic core, the difference between the vertical normal stress rapidly diminish. This implies that the shear function does play an important role. Overall, the patterns shown in Fig.4e (i.e. the difference in vertical normal stress) imply that the shear function exhibits similar depth-variation as does the vertical shear stress (recall that the former is related to the latter by the horizontal gradient). This inference is reasonable because, for instance, if the vertical shear stress above the elastic core is negligible in all columns throughout the outer-slope, so too are its horizontal gradients.

It may be useful at this point to consider an analogy between flexural and isostatic topography. In this analogy, the shear function can be thought of as an anomalous density with identical spatial localisation. So in our case, the concentration of the shear function within the elastic core, can be envisaged as an anomalous (increased) density in the same region. The integrated anomalous density sustains the elevation depression (relative to the reference location) and it also increases the local lithostatic gradient (relative to the same depth in the reference location). This increase in lithostatic gradient, diminishes the horizontal gradient in vertical normal stress which is present due to the elevation difference. It is widely appreciated that in the case of isostatic topography, the magnitude of the GPE depends on the vertical depth distribution of the density anomalies. Flipping our analogy around implies that exactly the same relationship applies in the case of flexural topography.

A simple estimate of GPE magnitude can be made by considering the contribution of the stress differences above the neutral plane depth. In the case of the numerical model, at the location x_s, the flexural topography (w) is ~ 1 km, giving $\Delta\sigma_{yy}$ $\sim$30 MPa. This stress difference, multiplied by the neutral plane depth ($z_n = 32$ km), gives a GPE difference of ~ 1 TN m^{-1}. This simple estimate compares reasonably well (albeit slightly conservatively) to the computed value (1.28 TN m^{-1}) derived by integrating the full stress difference (thick black line Fig.4e) across the entire lithosphere. Clearly there is some contribution to the GPE difference arising from the part of lithosphere beneath the elastic core. Indeed the normal stresses only fully equilibrate at a depth of 60 – 70 km, consistent with the mechanical thickness of the lithosphere (approximately twice the neutral plane depth).

4 Discussion

In the model analysed in this study, a ~ 5000 km SP experiences a total basal resisting force of about ~ 4 TN m^{-1}. The driving force to overcome this resistance is predominantly supplied by differences in gravitational potential energy (GPE) between ridge and trench. The trench GPE and the GPE due to density-induced subsidence (ridge push) are of a similar order (a few TN m^{-1}); the latter is reduced by the effect of dynamic topography, which acts as a subducting resisting force. This study shows that trench GPE is controlled by: 1) the amplitude of the downbending (w); and 2) stress patterns in the bending plate – specifically the depth at which Q is localised. Vertical shear stress, as well as the horizontal gradients thereof (i.e. Q), are maximal within the elastic core.

Previous studies have discussed the potential role of a strong plate core for subduction dynamics – envisaged primarily in its capacity to transmit a net in-plane force (e.g. Capitanio et al., 2009). In contrast, this study highlights the role of the elastic core in supporting vertical shear stresses. The reason the largest vertical shear stresses are found in the elastic core is not because of disproportionate strength *per se*, rather it is because principal stresses undergo 90° rotation across the core. This characteristic behaviour of bending plates is discussed further in the Supplementary Information. The elastic core depth, which is fundamentally related to the strength distribution of the lithosphere (Sandiford and Craig, 2023), mediates the translation of downbending (predominantly related to vertical shear and bending moments) to horizontal (GPE-related) forces.

In the model, the net in-plane force at the trench (F_{net}) is quite small: ~ 0.5 TN m^{-1}. At the outer rise F_{net} has increased to about 2.8 TN m^{-1}. Previous modelling studies, in which deviatoric tension in the SP was attributed to “net slab pull” have probably – at least to some degree – been detecting the effect of trench

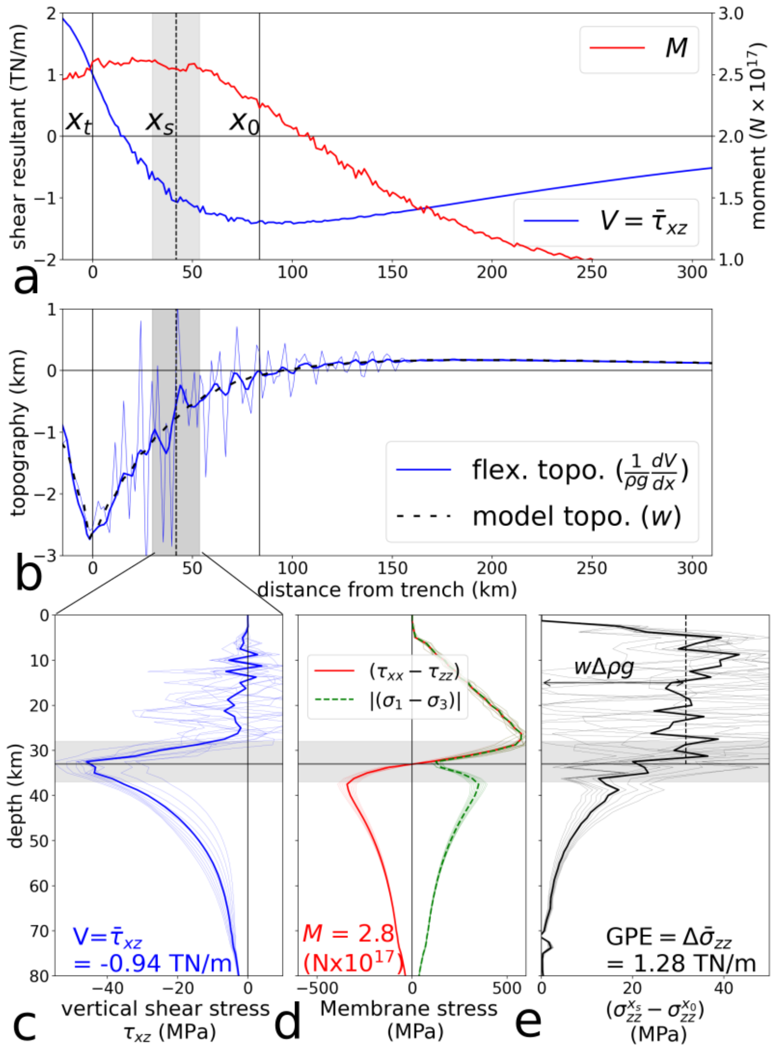

Figure 4: Stress patterns in the SP near the trench. All values are estimated by interpolating (and integrating) directly from the numerical model. (a) shows the horizontal variation in the vertical shear stress resultant (V) and the bending moment (M). The labelled vertical lines show the trench location (x_t), the first zero crossing (x_0), and a point that lies halfway between, in the outer slope (x_s), where the depth variation of stresses are investigated; (b) shows the predicted flexural topography (e.g. Eq. 7) and compares this to the model topography. The thin blue line is the unfiltered gradient, the thick blue line shows the same estimate with a Gaussian filter of length 1; (c) shows the distribution of the vertical shear stress, averaged over a small region around x_s (from multiple samples interpolated across the gray region shown in (b)); (d) shows the distribution of the membrane stress in red ($\sigma_{xx} - \sigma_{zz}$) and the magnitude of the differential stress in green ($\sigma_1 - \sigma_3$). The elastic core is highlighted with the horizontal grey band; (e) shows the difference in the vertical normal stress between x_s and x_0. The difference in normal stress reduces rapidly in the elastic core, and equilibrates fully at about twice the neutral plane depth.

GPE (Schellart, 2004; Capitanio et al., 2010; Sandiford et al., 2020). The model shows that net slab pull may not be necessary in order for mantle slabs to drive plates. Rather, what is observed might instead be referred to as “trench pull”. The trench is a very localised potential low, and acts like an idealised edge force. The plate responds to this force by developing net deviatoric tension. This reserve of extensional stress is used to pull the plate through a regions of stationary GPE change (d2, Fig. 3). While basal shear stress varies smoothly, the GPE is lumpy; the strength of the plate mediates rigid motions across these potential energy variations, through changes in F_{net}. Overall, the model dynamics resonate with the summary of Bercovici et al. (2015): “the pull of a slab on a plate is in fact a horizontal pressure gradient ...

caused by the low pressure associated with a slab pulling away from the surface … so that the boundary layer or plate feeds the slab steadily and thus leads to the appearance that the slab is pulling the plate." (see also Coltice et al. (2019)).

While the bending plate reaches moment-saturation (e.g. Fig. 4a), it is far from the upper-limit of F_{net}. This concurs with global patterns in SP seismicity – earthquakes being prevalent in the outer slope, but generally sparse seaward of the outer rise (Stein and Pelayo, 1991). That pattern, in turn, represents a problem for models of very high slab-plate coupling, where net slab pull must be close, or indeed limited, by SP strength (e.g. Conrad and Lithgow-Bertelloni, 2002; Zhang et al., 2023).

The deepest trenches on Earth, within the Marianas system, reach 4-6 km depth relative to the incoming plate (Zhou et al., 2015; Zhang et al., 2023). Supposing the neutral plane depth reaches a maximum of 35 km (Craig et al., 2014; Sandiford and Craig, 2023), and using a trench depth of 6 km, an estimated maximum trench GPE, would be ~ 5 TN m^{-1} (based on the relationships highlight in the previous section). Zhou et al. (2015) have argued that the trenchward-dipping outer-slope faulting pattern in the Marianas region, requires a net in-plane force of about 5 TN m^{-1}. Their models do not include body forces, and hence while they produce flexural deformation, it is not coupled to GPE. It could be that the net-plane force is simply an expression of the deviatoric tension due to the trench GPE.

Finally, the subduction model motivates consideration of the role of dynamic topography and its impact on driving forces. In the 2D model discussed here, the dynamic topography is controlled by an asthenosphere pressure gradient, and the slope acts as a resisting force on the SP. At a global scale, the presence of this SP signal is ambiguous (Holt, 2022). One possibility is that any signal of slab driven pressure gradients are subordinate to a larger signal. Both tomographic and residual topography models reveal a consistent long-wavelength (degree 1-3) pattern, with positive anomalies in South Pacific paired with a negative anomalies in East Asia (Steinberger et al., 2001; Hoggard et al., 2017), which are consistent with the history of subduction (Ricard et al., 1993). If the residual topography is interpreted as dynamic topography, the Pacific Plate would experience a generally WNW slope, with an total amplitude of perhaps 0.5-1 km, across distances on the order of 5000 km (Davies et al., 2023). In that case the GPE due to isostatic subsidence, the dynamic topography and trench GPE would all act to drive the plate in a generally westwards direction. If basal shear is sufficient to balance the sum of those forces, the intraplate stresses would remain near-neutral. If the basal shear cannot balance them, or is in fact an additional net driving force (Steinberger et al., 2001; Stotz et al., 2018), the Pacific Plate should enter deviatoric compression as it moves from the GPE highs to lows. This has been predicted for NW Pacific in several global-scale convection models (Steinberger et al., 2001; Ghosh and Holt, 2012; Yoshida and Zhou, 2023). In terms of the seismicity record, either of these possibilities are plausible (Wiens and Stein, 1983; Stein and Pelayo, 1991; Sandiford and Craig, 2023).

5 Conclusions

In this study I analyse the horizontal subducting plate force balance, based on stress fields derived from a numerical model. The driving force is predominantly supplied by differences in GPE between ridge and trench. The GPE associated with the trench, provides about 2.0 TN m^{-1} net driving force, while the net in-plane force at the trench is ~ 0.5 TN m^{-1}. The GPE due to plate cooling and subsidence is reduced by almost a half (to about 1.5 TN m^{-1}) due to the effect of dynamic topography. I discuss how stress patterns in the SP, which are strongly mediated by bending, control the magnitude of the trench GPE. For the deepest trenches on Earth, these relationships imply trench GPE of up to about 5 TN m^{-1}. Hence mantle slabs can drive plate tectonics simply through the capacity downbend the plate – i.e through supplying a vertical shear stress and bending moment at the trench – rather than by a net in-plane force. Trenches will still act as plate attractors and lead to the appearance that the slab is pulling the plate.

Appendix 1

Thin plate description of the horizontal force balance

The thin-plate analysis starts with equilibrium equations (e.g. Eq. 10), where dimensions are force per unit volume, and then integrates these over a sub-region that encompasses the plate. Following integration, we have terms that a describe a balance of horizontal forces, with dimensions of $\mathrm{N\,m^{-1}}$ or force per unit distance in the out of plane direction. Starting with the horizontal stress equilibrium:

$$\frac{\partial \sigma_{xx}}{\partial x} + \frac{\partial \sigma_{xz}}{\partial z} = 0 \tag{9}$$

$$\frac{\partial \tau_{xx}}{\partial x} - \frac{\partial P}{\partial x} + \frac{\partial \tau_{xz}}{\partial z} = 0 \tag{10}$$

We will now vertically integrate Eq. 10, from the plate surface $s(x)$ down to a reference LAB level L (in practice L is chosen as 125 km beneath the mean surface elevation):

$$\int_L^{s(x)} \frac{\partial \tau_{xx}}{\partial x} dz - \int_L^{s(x)} \frac{\partial P}{\partial x} dz + \int_L^{s(x)} \frac{\partial \tau_{xz}}{\partial z} dz = 0 \tag{11}$$

Now, denote the vertical integration with an overbar, and chanage the order of the derivatives/integrals:

$$\frac{\partial}{\partial x}(\bar{\tau}_{xx} - \bar{P}) + \sigma_{xz}|_L = 0 \tag{12}$$

This step has assumed a stress free surface. Now, we write P in terms of the definition of the vertical stress:

$$\bar{\sigma}_{zz} - \bar{\tau}_{zz} = -\bar{P} \tag{13}$$

Substituting into Eq. 12 and rearranging terms:

$$\frac{\partial}{\partial x}(\bar{\tau}_{xx} - \bar{\tau}_{zz}) + \frac{\partial}{\partial x}(\bar{\sigma}_{zz}) + \tau_{xz}|_L = 0 \tag{14}$$

This is the horizontal force balance, vertically integrated across a given depth. Positive gradients indicate forces to the right. We now integrate 16 over a horizontal section of the lithosphere:

$$\int_{x_t}^{x} \sigma_{xz}\Big|_L dx = -(\bar{\sigma}_{zz})\Big|_{x_t}^{x} - (\bar{\tau}_{xx} - \bar{\tau}_{zz})\Big|_{x_t}^{x} \tag{15}$$

$$= -\Delta(\bar{\sigma}_{zz}) - \Delta(\bar{\tau}_{xx} - \bar{\tau}_{zz}) \tag{16}$$

And finally, define the GPE as the negative of the vertically integrated normal stress, so that a positive change in GPE (to the right) indicates a net a force acting the left. This final definition has no physical relevance, it is simply a convenience related to plotting:

$$\int_{x_t}^{x} \sigma_{xz}\Big|_L dx = \Delta(GPE) - \Delta(F_{net}) \tag{17}$$

Acknowledgements

The numerical model discussed in this work was developed with support by Australian Research Council grants DP150102887 and DP180102280, and with the assistance of resources and services from the National Computational Infrastructure (NCI), which is supported by the Australian Government. The Computational Infrastructure for Geodynamics (geodynamics.org) which is funded by the National Science Foundation under award EAR-0949446 and EAR-1550901, is acknowledged for supporting the development of ASPECT. Analysis was facilitated by the Pyvista library Sullivan and Kaszynski (2019).

Data availability

Input files and a description of code modifications to reproduce the numerical model can be found at https://github.com/dansand/subduction_GJI2022.

References

Bangerth, W., Dannberg, J., Fraters, M., Gassmoeller, R., Glerum, A., Heister, T., Myhill, R., and Naliboff, J. (2023). ASPECT: Advanced Solver for Problems in Earth's ConvecTion, User Manual. doi:10.6084/m9.figshare.4865333.

Bangerth, W., Dannberg, J., Gassmoeller, R., and Heister, T. (2020). Aspect v2.2.0.

Becker, T. W. and O'Connell, R. J. (2001). Predicting plate velocities with mantle circulation models. *Geochemistry, Geophysics, Geosystems*, 2(12).

Bercovici, D., Tackley, P., and Ricard, Y. (2015). 7.07-the generation of plate tectonics from mantle dynamics. *Treatise on Geophysics. Elsevier, Oxford*, pages 271–318.

Bird, P., Liu, Z., and Rucker, W. K. (2008). Stresses that drive the plates from below: Definitions, computational path, model optimization, and error analysis. *Journal of Geophysical Research: Solid Earth*, 113(B11).

Bueler, E. and Brown, J. (2009). Shallow shelf approximation as a "sliding law" in a thermomechanically coupled ice sheet model. *Journal of Geophysical Research: Earth Surface*, 114(F3).

Buffett, B. and Becker, T. (2012). Bending stress and dissipation in subducted lithosphere. *Journal of Geophysical Research: Solid Earth*, 117(B5).

Byerlee, J. (1978). Friction of rocks. *Rock friction and earthquake prediction*, pages 615–626.

Caldwell, J., Haxby, W., Karig, D. E., and Turcotte, D. (1976). On the applicability of a universal elastic trench profile. *Earth and Planetary Science Letters*, 31(2):239–246.

Capitanio, F. A., Morra, G., and Goes, S. (2007). Dynamic models of downgoing plate-buoyancy driven subduction: Subduction motions and energy dissipation. *Earth and Planetary Science Letters*, 262(1-2):284–297.

Capitanio, F. A., Morra, G., and Goes, S. (2009). Dynamics of plate bending at the trench and slab-plate coupling. *Geochemistry, Geophysics, Geosystems*, 10(4).

Capitanio, F. A., Stegman, D. R., Moresi, L.-N., and Sharples, W. (2010). Upper plate controls on deep subduction, trench migrations and deformations at convergent margins. *Tectonophysics*, 483(1-2):80–92.

Clennett, E. J., Holt, A. F., Tetley, M. G., Becker, T. W., and Faccenna, C. (2023). Assessing plate reconstruction models using plate driving force consistency tests. *Scientific Reports*, 13(1):10191.

Coblentz, D. D., Richardson, R. M., and Sandiford, M. (1994). On the gravitational potential of the earth's lithosphere. *Tectonics*, 13(4):929–945.

Coltice, N., Husson, L., Faccenna, C., and Arnould, M. (2019). What drives tectonic plates? *Science advances*, 5(10):eaax4295.

Conrad, C. P. and Lithgow-Bertelloni, C. (2002). How mantle slabs drive plate tectonics. *Science*, 298(5591):207–209.

Copley, A., Avouac, J.-P., and Royer, J.-Y. (2010). India-asia collision and the cenozoic slowdown of the indian plate: Implications for the forces driving plate motions. *Journal of Geophysical Research: Solid Earth*, 115(B3).

Craig, T., Copley, A., and Jackson, J. (2014). A reassessment of outer-rise seismicity and its implications for the mechanics of oceanic lithosphere. *Geophysical Journal International*, 197(1):63–89.

Davies, D. R., Ghelichkhan, S., Hoggard, M., Valentine, A. P., and Richards, F. D. (2023). Observations and models of dynamic topography: Current status and future directions. *Dynamics of Plate Tectonics and Mantle Convection*, pages 223–269.

Davies, G. F. (1978). The roles of boundary friction, basal shear stress and deep mantle convection in plate tectonics. *Geophysical Research Letters*, 5(3):161–164.

Elasasser, W. M. (1969). Convection and stress propagation in the upper mantle. *The application of modern physics to the Earth and planetary interiors*, pages 223–246.

England, P. and Molnar, P. (2022). Changes in plate motions caused by increases in gravitational potential energy of mountain belts. *Geochemistry, Geophysics, Geosystems*, 23(10):e2022GC010389.

Faccenna, C., Becker, T. W., Lallemand, S., and Steinberger, B. (2012). On the role of slab pull in the cenozoic motion of the pacific plate. *Geophysical Research Letters*, 39(3).

Forsyth, D. and Uyeda, S. (1975). On the relative importance of the driving forces of plate motion. *Geophysical Journal International*, 43(1):163–200.

Garcia, E. S. M., Sandwell, D. T., and Bassett, D. (2019). Outer trench slope flexure and faulting at pacific basin subduction zones. *Geophysical Journal International*, 218(1):708–728.

Ghosh, A. and Holt, W. E. (2012). Plate motions and stresses from global dynamic models. *Science*, 335(6070):838–843.

Goetze, C. and Evans, B. (1979). Stress and temperature in the bending lithosphere as constrained by experimental rock mechanics. *Geophysical Journal International*, 59(3):463–478.

Heister, T., Dannberg, J., Gassmöller, R., and Bangerth, W. (2017). High accuracy mantle convection simulation through modern numerical methods. II: Realistic models and problems. *Geophysical Journal International*, 210(2):833–851.

Hirth, G. and Kohlstedt, D. (2003). Rheology of the upper mantle and the mantle wedge: A view from the experimentalists. *Geophysical monograph-american geophysical union*, 138:83–106.

Hoggard, M. J., Winterbourne, J., Czarnota, K., and White, N. (2017). Oceanic residual depth measurements, the plate cooling model, and global dynamic topography. *Journal of Geophysical Research: Solid Earth*, 122(3):2328–2372.

Holt, A. F. (2022). The topographic signature of mantle pressure build-up beneath subducting plates: Insights from spherical subduction models. *Geophysical research letters*, 49(22):e2022GL100330.

Holt, A. F. and Becker, T. W. (2016). The effect of a power-law mantle viscosity on trench retreat rate. *Geophysical Journal International*, page ggw392.

Hunter, J. and Watts, A. (2016). Gravity anomalies, flexure and mantle rheology seaward of circum-pacific trenches. *Geophysical Journal International*, 207(1):288–316.

Husson, L. (2012). Trench migration and upper plate strain over a convecting mantle. *Physics of the Earth and Planetary Interiors*, 212:32–43.

Kronbichler, M., Heister, T., and Bangerth, W. (2012). High accuracy mantle convection simulation through modern numerical methods. *Geophysical Journal International*, 191:12–29.

McKenzie, D. P. (1969). Speculations on the consequences and causes of plate motions. *Geophysical Journal International*, 18(1):1–32.

Mei, S., Suzuki, A., Kohlstedt, D., Dixon, N., and Durham, W. (2010). Experimental constraints on the strength of the lithospheric mantle. *Journal of Gmersoneophysical Research: Solid Earth*, 115(B8).

Osei Tutu, A., Steinberger, B., Sobolev, S. V., Rogozhina, I., and Popov, A. A. (2018). Effects of upper mantle heterogeneities on the lithospheric stress field and dynamic topography. *Solid Earth*, 9(3):649–668.

Parsons, B. and Molnar, P. (1976). The origin of outer topographic rises associated with trenches. *Geo-*

physical Journal International, 45(3):707–712.

Ricard, Y., Richards, M., Lithgow-Bertelloni, C., and Le Stunff, Y. (1993). A geodynamic model of mantle density heterogeneity. *Journal of Geophysical Research: Solid Earth*, 98(B12):21895–21909.

Richardson, R. M. (1992). Ridge forces, absolute plate motions, and the intraplate stress field. *Journal of Geophysical Research: Solid Earth*, 97(B8):11739–11748.

Richardson, R. M., Solomon, S. C., and Sleep, N. H. (1976). Intraplate stress as an indicator of plate tectonic driving forces. *Journal of geophysical research*, 81(11):1847–1856.

Rowley, D. B. and Forte, A. M. (2022). Kinematics of the east pacific rise retrodicted from pacific and farallon/nazca subduction-related torques: Support for significant deep mantle buoyancy controlling epr spreading. *Journal of Geophysical Research: Solid Earth*, 127(2):e2020JB021638.

Royden, L. H. and Husson, L. (2006). Trench motion, slab geometry and viscous stresses in subduction systems. *Geophysical Journal International*, 167(2):881–905.

Sandiford, D. and Craig, T. J. (2023). Plate bending earthquakes and the strength distribution of the lithosphere. *Geophysical Journal International*, 235(1):488–508.

Sandiford, D. and Moresi, L. (2019). Improving subduction interface implementation in dynamic numerical models. *Solid Earth*, 10(3):969–985.

Sandiford, D., Moresi, L., Sandiford, M., Farrington, R., and Yang, T. (2020). The fingerprints of flexure in slab seismicity. *Tectonics*, 39(8):e2019TC005894.

Sandiford, M., Coblentz, D., and Schellart, W. P. (2005). Evaluating slab-plate coupling in the indo-australian plate. *Geology*, 33(2):113–116.

Schellart, W. (2004). Quantifying the net slab pull force as a driving mechanism for plate tectonics. *Geophysical research letters*, 31(7).

Schmalholz, S. M., Medvedev, S., Lechmann, S. M., and Podladchikov, Y. (2014). Relationship between tectonic overpressure, deviatoric stress, driving force, isostasy and gravitational potential energy. *Geophysical Journal International*, 197(2):680–696.

Schubert, G., Yuen, D. A., Froidevaux, C., Fleitout, L., and Souriau, M. (1978). Mantle circulation with partial shallow return flow: Effects on stresses in oceanic plates and topography of the sea floor. *Journal of Geophysical Research: Solid Earth*, 83(B2):745–758.

Solomon, S. C. and Sleep, N. H. (1974). Some simple physical models for absolute plate motions. *Journal of Geophysical Research*, 79(17):2557–2567.

Stein, S. and Pelayo, A. (1991). Seismological constraints on stress in the oceanic lithosphere. *Philosophical Transactions of the Royal Society of London. Series A: Physical and Engineering Sciences*, 337(1645):53–72.

Steinberger, B. and Calderwood, A. R. (2006). Models of large-scale viscous flow in the earth's mantle with constraints from mineral physics and surface observations. *Geophysical Journal International*, 167(3):1461–1481.

Steinberger, B., Schmeling, H., and Marquart, G. (2001). Large-scale lithospheric stress field and topography induced by global mantle circulation. *Earth and Planetary Science Letters*, 186(1):75–91.

Stotz, I., Iaffaldano, G., and Davies, D. R. (2018). Pressure-driven poiseuille flow: a major component of the torque-balance governing pacific plate motion. *Geophysical Research Letters*, 45(1):117–125.

Suchoy, L., Goes, S., Maunder, B., Garel, F., and Davies, R. (2021). Effects of basal drag on subduction dynamics from 2d numerical models. *Solid Earth*, 12(1):79–93.

Sullivan, C. and Kaszynski, A. (2019). Pyvista: 3d plotting and mesh analysis through a streamlined interface for the visualization toolkit (vtk). *Journal of Open Source Software*, 4(37):1450.

Turcotte, D. L., McAdoo, D., and Caldwell, J. (1978). An elastic-perfectly plastic analysis of the bending of the lithosphere at a trench. *Tectonophysics*, 47(3-4):193–205.

Turcotte, D. L. and Schubert, G. (2002). *Geodynamics*. Cambridge university press.

van Summeren, J., Conrad, C. P., and Lithgow-Bertelloni, C. (2012). The importance of slab pull and a global asthenosphere to plate motions. *Geochemistry, Geophysics, Geosystems*, 13(2).

Watts, A. and Talwani, M. (1974). Gravity anomalies seaward of deep-sea trenches and their tectonic implications. *Geophysical Journal International*, 36(1):57–90.

Whittaker, A. (1988). *A numerical study of the dynamics of subduction*. PhD thesis, Durham University.

Wiens, D. A. and Stein, S. (1983). Age dependence of oceanic intraplate seismicity and implications for lithospheric evolution. *Journal of Geophysical Research: Solid Earth*, 88(B8):6455–6468.

Wortel, M., Remkes, M., Govers, R., Cloetingh, S., and Meijer, P. T. (1991). Dynamics of the lithosphere and the intraplate stress field. *Philosophical Transactions of the Royal Society of London. Series A: Physical and Engineering Sciences*, 337(1645):111–126.

Wouters, M. C., Pérez-Díaz, L., Tuck-Martin, A., Eagles, G., Adam, J., and Govers, R. (2021). Dynamics of the african plate 75 ma: From plate kinematic reconstructions to intraplate paleo-stresses. *Tectonics*, 40(7).

Yoshida, M. and Zhou, Z. (2023). Stress state of the stable part of the pacific plate predicted by a numerical model of global mantle flow coupled with plate motion. *Lithosphere*, 2023(1).

Zhang, J., Yang, H., Zhu, G., Chen, H., Zhang, F., and Sun, Z. (2023). The effect of along-strike variable plate deflection on bending stress and seismicity at the southern mariana trench. *Tectonophysics*, 850:229752.

Zhou, Z., Lin, J., Behn, M. D., and Olive, J.-A. (2015). Mechanism for normal faulting in the subducting plate at the mariana trench. *Geophysical Research Letters*, 42(11):4309–4317.